Effect of Improved Area Ratio of Deep Mixing Wall Grid on Pile Stress in Piled Raft System under Strong Earthquakes

深層混合処理による格子壁の改良率が大地震時のパイルド・ラフト基礎の杭応力に及ぼす影響

Kiyoshi Yamashita 山下 清*1 Yoshimasa Shigeno 重野 喜政*2 Junji Hamada 濱田 純次*3

Summary

The recent research on seismic response analysis of piled raft with grid-form deep mixing walls (DMWs) has demonstrated that the DMWs are quite effective at reducing the sectional forces of the piles to an acceptable level in soft ground. In this paper, to investigate the influence of an improved area ratio on pile bending moment in a piled raft system, nonlinear seismic response analyses using three-dimensional finite elements under Level 2 earthquakes are conducted. Two different geometries of the DMW grid are considered, i.e., the area ratios are 25% (16 square cells) and 16% (4 square cells). Consequently, it was found that the maximum bending moments in the cases with four cells are significantly below the ultimate limit state under Level 2 seismic motion, while those in the cases with 16 cells are fairly below the damage limit state as presented in the previous study.

Keywords: piled raft foundation, grid-form deep mixing walls, strong earthquake, 3-dimensional FE analysis, tensile failure, performance-based design

梗　概

軟弱地盤にあるパイルド・ラフト基礎において，大地震時に杭に生じる応力が格子状深層混合改良壁により大幅に低減されることが最近の研究で指摘されている。本文では，杭に生じる最大曲げモーメントと格子壁の改良率の関係を調べるために，改良率の異なる2つの格子壁（改良率25%（16格子）と16%（4格子））について，レベル2地震動の下で3次元FEモデルを用いた非線形時刻歴応答解析を実施した。その結果，杭に生じる曲げモーメントの最大値は，16格子のとき損傷限界状態に相当する値よりかなり小さいこと，4格子の場合は16格子の場合と比べてやや大きくなるが，終局限界状態に対して十分な余裕があることが判明した。

キーワード：パイルド・ラフト基礎，格子状地盤改良，大地震，3次元FE解析，引張り破壊，性能設計

1 INTRODUCTION

The effectiveness of piled rafts in reducing overall and differential settlements has been confirmed not only in favorable ground conditions, as reported by Katzenbach et al. (2000), Poulos (2001) and Mandolini et al. (2005), but also in unfavorable ground conditions with ground improvement technique as in the case histories reported by Yamashita et al. (2011a, 2011b, 2013). It has been also recognized that piled rafts would be resilient against seismic events. For example, Yamashita et al. (2012, 2016, 2017) have reported that the piled raft with the grid-form deep mixing walls (DMWs) in soft ground supporting mid-rise buildings showed excellent seismic performance during and after the 2011 off the Pacific coast of Tohoku Earthquake (M_w=9.0). Furthermore, the recent research on seismic response analysis of a piled raft with grid-form DMWs using a three-dimensional nonlinear finite element model has shown that the DMWs are quite effective at reducing the sectional forces of the piles to an acceptable level in soft ground under strong earthquakes, based on the successful seismic simulation using the

＊1 Executive Manager, Research & Development Institute, Dr. Eng. 技術研究所 専門役 博士（工学）
＊2 Group Leader, Research & Development Institute 技術研究所 先端技術研究部 数理科学グループ長
＊3 Group Leader, Research & Development Institute, Dr. Eng. 技術研究所 地盤・基礎部 基礎構造グループ長 博士（工学）

moderate motion recorded during the 2011 Tohoku Earthquake (Yamashita et al., 2018).

The grid-form DMWs can be designed more rationally using the principles of performance-based design (PBD) as pointed by Namikawa et al. (2007). In other words, if the grid-form DMWs were designed to reinforce the seismic resistance of piled raft foundation, it would be rational that minor damages of the DMWs are allowed under the seismic forces of interest. Notwithstanding the required levels of the foundation performance should be examined carefully in such design that the effects of partial damage of the DMWs on the behavior of piles enclosed by them are considered. Bradley et al. (2013) have investigated the effect of various configurations of lattice-shaped soil improvement on the seismic response of liquefiable soil deposits using 3-dimentional seismic effective stress analysis.

In this paper, in order to investigate cost performance effectiveness of the DMW grids, the influence of the improved area ratio (area of the DMWs in plan divided by the total area) on pile bending moment in a piled raft system is examined. Seismic response analysis of the piled raft system supporting a 12-story base-isolated building is conducted using the same three-dimensional finite element model as in the previous study, taking into account of two different geometries of the DMW grid in which the improved area ratios are 25 and 16%. Through the dynamic analysis, the effectiveness of the DMW grids with the different area replacement ratios on reducing the sectional force of the piles was examined, and the internal stresses induced in the DMWs were also discussed.

2 CASE HISTORY OF 12-STORY BUILDING

Figure 1 illustrates a schematic view of the building and its foundation with a typical soil profile (Yamashita et al., 2012). The building is a 12-story reinforced-concrete structure located in Tokyo and the total load in the structural design was 198.8 MN. The building has a seismic base-isolation system which consists of base isolators (laminated rubber bearings) and damper (oil damper and mechanical damper). The natural period of the base-isolation system is 4.6 s in the NS direction when the base isolation devices fully function against Level 2 seismic motions in Japan, while the fixed based natural period of the superstructure is 0.96 s. The soil down to a depth of 43 m is an alluvial stratum. The upper 7m is fill, soft silt and loose silty sand. The rest is very soft to medium silty clay. Below the depth of 46 m, there are dense sand to a depth of 48 m, underlain by very dense sand and gravel. The building is supported by a piled raft with grid-form DMWs which were employed to prevent the liquefaction of the silty sand from a depth of 3 to 7 m as well as to improve the bearing capacity beneath the raft.

Figure 2 illustrates the foundation plan with the locations of the monitoring devices. The ground improvement execution was carried out by the Cement Deep Mixing machine equipped with four mixing shafts. The spacing of the mixing shafts was 0.8 m for the diameter of mixing blades of 1.0 m. The DMW grid has 16 square cells in a four-by-four pattern and the improved area ratio (A_r) is 25%. Furthermore, to improve the bearing capacity of the raft foundation, the DMWs were extended to a depth of 16 m with the bottom being embedded in stiffer silty clay. Sixteen 45-m-long piles, which consist of SC (steel pipe-concrete

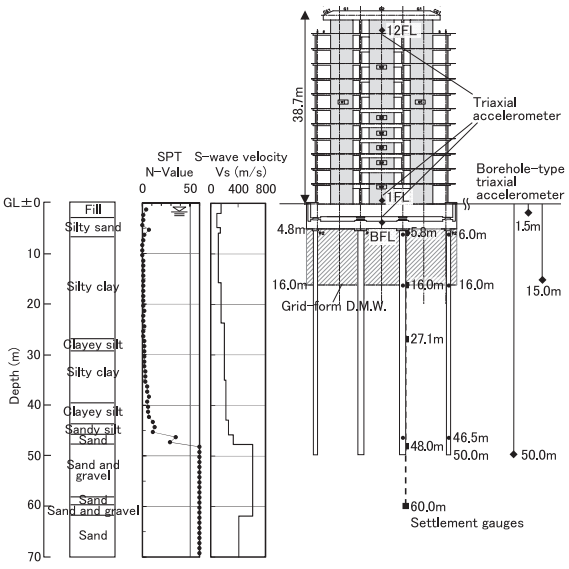

Fig. 1 Schematic of the building and foundation with soil profile

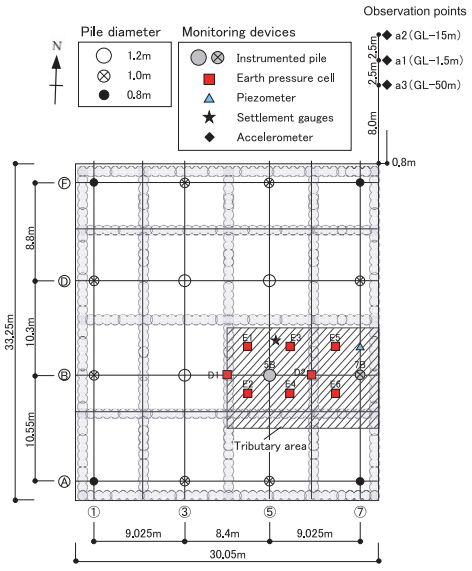

Fig. 2 Foundation plan with locations of monitoring devices

composite) pile in the top portion and PHC (pretensioned spun high-strength concrete) pile in the rest, 0.8-1.2 m in diameter, were used to reduce the settlement to acceptable levels. The pile toes reached the very dense sand-and-gravel layer.

3 3-D FINITE ELEMENT MODEL

3.1 Soil-structure system and geometries of DMW grid

Figure 3 illustrates the three-dimensional finite element model of soil-foundation-superstructure for simulation analysis of the twelve-story building mentioned on the above. The lateral boundaries are periodic boundaries, while the bottom boundary is a viscous one. The piles were modeled using beam elements and void with rigid bar elements to consider the shape and volume of the piles as illustrated in Fig. 3(b). Table 1 shows the material properties of the piles. The horizontal load vs. displacement relation of the base isolators was modeled using a tri-linear spring (Hamada et al., 2014).

Figure 4 illustrates a plan view of the grid-form DMWs and Piles 5B and 7B (monitored piles). Two different geometries of the DMW grid were considered. One is a case in which the grid had 16 square cells which is consistent with the case in the twelve-story building. The other is a case in which the grid had four square cells. The improved area ratio of the former is 25% and that of the latter is 16%. In addition, numerical cases without DMWs were also studied.

The software is an in-house program called MuDIAN (Shiomi et al., 1993). It is parallelized using the hybrid parallel method, and able to analyze a large-DOF (degree of freedom) model at high speed (Shigeno et al., 2014).

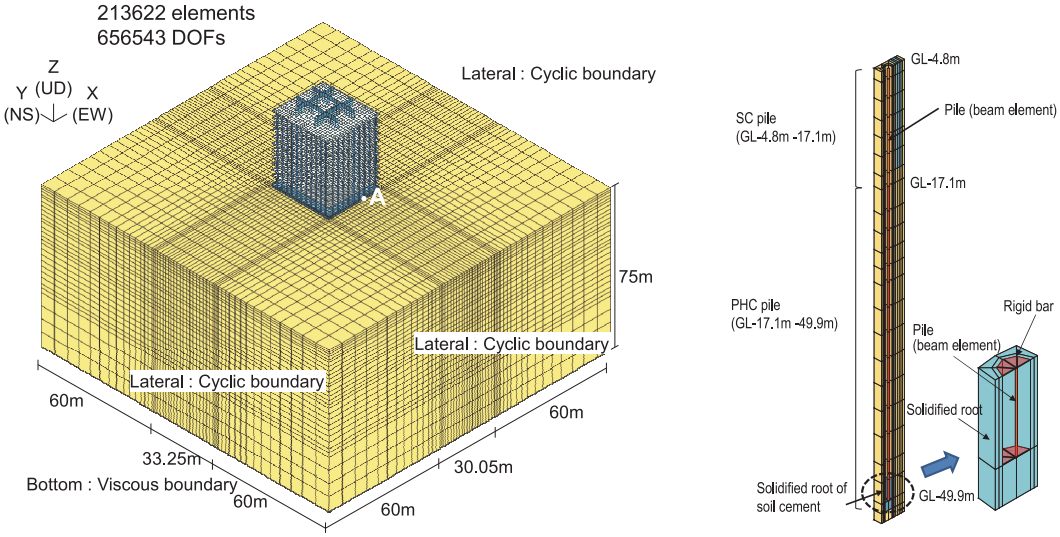

(a) Ground and structure (b) Pile

Fig. 3 Finite element model of soil-foundation-structure

Table 1 Dimensions and material properties of piles

Pile diameter (mm)	Young's modulus (MPa)	Density ρ (t/m^3)	Damping ratio (%)	A_e of SC pile (m^2)	I_e of SC pile (m^4)	A_e of PHC pile (m^2)	I_e of PHC pile (m^4)
800	40000	2.5	2.0	0.3268	0.02199	0.2441	0.01455
1000	40000	2.5	2.0	0.4649	0.04899	0.3633	0.03437
1200	40000	2.5	2.0	0.6714	0.10316	0.5054	0.06958

A_e : Equivalent cross-sectional area
I_e : Equivalent area moment of inertia

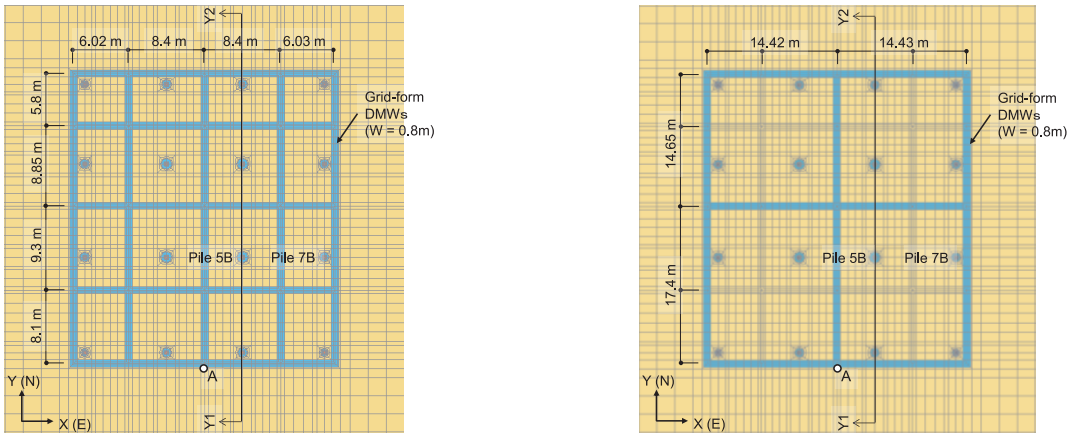

(a) 16 cells (A_r=25%) (b) 4 cells (A_r=16%)

Fig. 4 Plan view of DMW grid and piles

3.2 Modelling of soil and stabilized soil

As the three-dimensional constitutive model of soil, the Yoshida model for multi-dimensional analyses was used (Tsujino et al., 1994). The Yoshida model is a two-surface model using a yielding surface and a loading surface which describes the state of the current stress. The Mohr-Coulomb model was used as the yielding surface that provides the strength of the soil. The stress-strain relationship in the present soil model is based on a nonlinear elastic model and the yielding function is only used as a strength criterion. The skeleton curve of the model is derived discretely using the normalized shear modulus vs. shear strain relationship (G/G_0-γ). The damping characteristic is obtained by combining Masing's rule and the hyperbolic function. The parameters of the function are determined from the damping ratio vs. shear strain relationship (h-γ). Figure 5 shows the G/G_0-γ and h-γ characteristics of the soil obtained from cyclic triaxial tests on undisturbed samples. Figure 6 shows the shear wave velocity (V_s) profile derived from a P-S logging, together with the V_s profile used in the analysis. It should be noted that soil liquefaction is not considered in this analysis although the sandy soil layer between depths of 3 and 7 m may occur under strong earthquakes.

As the constitutive model of the stabilized soil, the Hayashi-Hibino model (Motojima et al., 1978) was used as a two criteria model. The Hayashi-Hibino model is a nonlinear elastic model which is capable of evaluating tensile and shear failure, and the elastic modulus is reduced to a user's specified value at failure. The criteria of the Hayashi-Hibino model are shown in Fig. 7. The tensile strength is evaluated correctly by taking the lower strength between the two criteria.

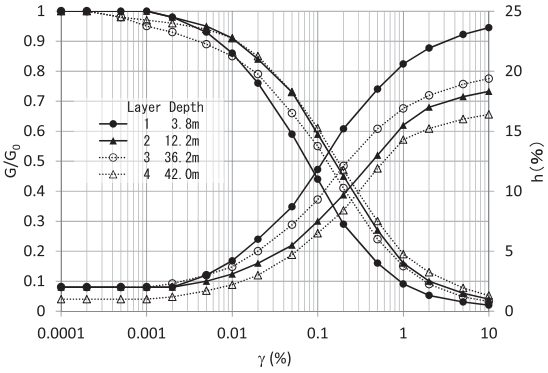

Fig. 5 Strain-dependent characteristics of unimproved soil

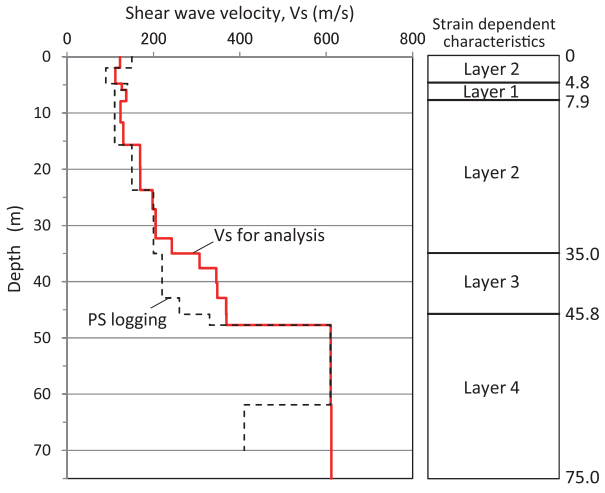

Fig. 6 Profile of optimized initial shear wave velocity and strain dependence characteristics in analysis

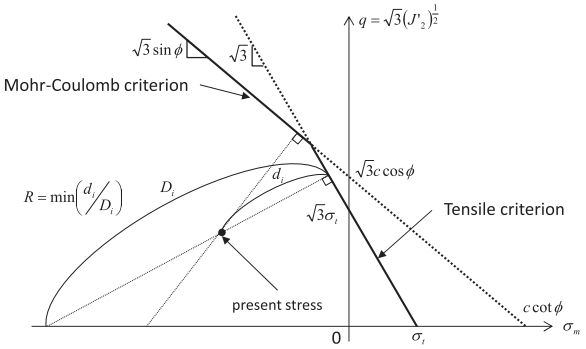

Fig. 7 Criteria of Hayashi-Hibino model

Table 2 Properties of stabilized soil and parameters used in Hayashi-Hibino model

Density ρ (t/m^3)	F_c	Tensile strength σ_t=0.2F_c (MPa)	Cohesion c=0.3F_c (MPa)	Friction angle ϕ (degree)	Initial shear modulus G_0 (MPa)	Poisson's ratio ν_0	Damping ratio h (%)	Nonlinear parameter a	G/G_0 after failure
2.0	2.6	0.52	0.78	30	500	0.26	5.0	1.0	1.0e-5

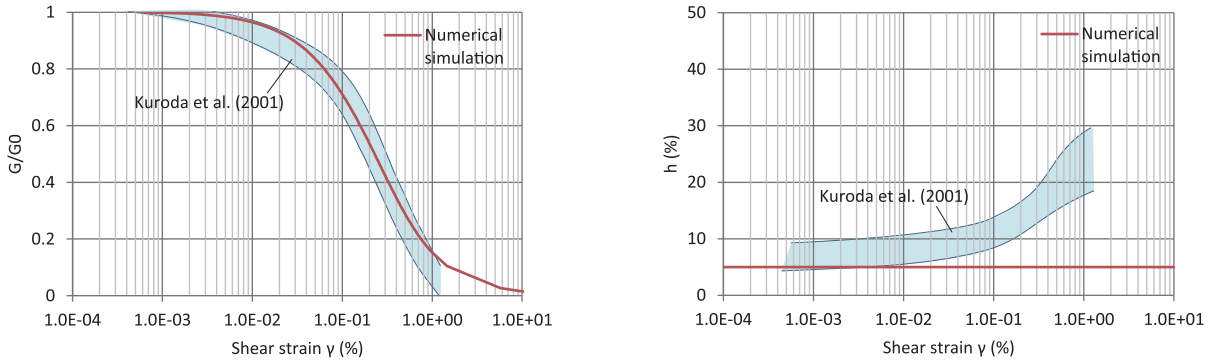

(a) G/G_0 (b) h

Fig. 8 Strain-dependent characteristics of stabilized soil

Table 2 shows the properties of the stabilized soil and the parameters used in the Hayashi-Hibino model. The tensile strength and cohesion were set to 0.2 F_c and 0.3 F_c, respectively, according to BCJ (2002) where F_c is the design standard strength. The value of F_c is given by Eq. (1) (BCJ, 2002; Kitazume, 2013).

$$F_c = \overline{q}_{uf} - K\sigma = (1 - 1.3V_{quf})\,\overline{q}_{uf} \quad (1)$$

where $\overline{q}_{uf}$ is the average value of q_{uf} (compressive strength of core samples of in-situ stabilized column) and set at 3.81 MPa based on the test results; σ is the standard deviation of q_{uf}; V_{quf} is coefficient of variation and set at 0.25; K is coefficient and set at 1.3. Then, F_c was calculated as 2.6 MPa. Figure 8 shows the shear modulus degradation curve and the damping used in the analysis. Note that since only the skeleton curve is modeled and the hysteresis is not included in the Hayashi-Hibino model, the Rayleigh damping was used. The initial shear modulus G_0 of 500 MPa was determined based on the calibration through a numerical simulation using the records of the 2011 Tohoku Earthquake. As for the initial stress in the DMWs, an isotropic stress of 170 kPa was assumed.

3.3 Input ground motion and numerical cases

As the strong earthquake motion for the present analysis, the code-defied artificial seismic motion called "Level 2 seismic motion" in Japan was used. The acceleration response spectra of Level 2 motion are compatible to that defined on the engineering bedrock shown in Fig. 9 (The Building Standard Law of Japan, 2000). Level 2 seismic motion may correspond to the design-basis earthquake for buildings with mean return period of 475 years (Verdugo, 2017). The input motions, which were generated using two sets of phase data, i.e., the Kobe and Hachinohe phase data, were applied horizontally at 75 m depth in the NS direction. Figure 10 shows the input accelerations of the Kobe and Hachinohe phase motions (the waves are 2E). The time interval and analysis time were 0.005 s and 120 s, respectively.

In total, six numerical cases, under Kobe and Hachinohe phase motions, are listed in Table 3. Note that Cases K16, H16, K0 and H0 correspond to Cases K1, H1, K2 and H2 presented in the previous study. Further details of the finite element analysis have been described in the previous paper (Yamashita et al., 2018).

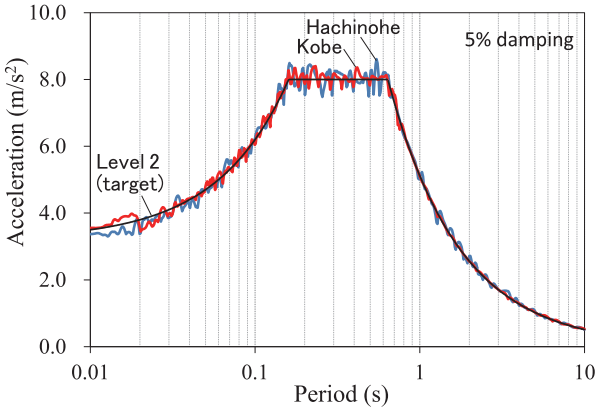

Fig. 9 Acceleration response spectra of Level 2 motions on bedrock

4 ANALYSIS RESULTS

4.1 Response of ground and piles

Figure 11 shows the peak horizontal displacement profiles of the ground at point A shown in Fig. 3(a) and the free field relative to the reference point (at a depth of 49.9 m). The ground displacements under the Kobe phase were generally greater than those under the Hachinohe phase. The ground displacements in the cases with four cells were slightly greater than those in the cases with 16 cells for both input motions, while the ground displacements in the cases with DMWs were fairly smaller than those without DMWs for both input motions.

Figure 12 illustrates the ground deformation with the contours of equivalent strain under Kobe phase motion in cross-section Y1-Y2 (shown in Fig. 4), when the horizontal displacement of the raft bottom at point A was at its absolute maximum (referred as t_D). The increase in equivalent strain in the cases with DMWs was significantly restrained within the DMW grids compared to that in the cases without DMWs. It is seen that the increase in strain in K4 was slightly greater than that in K16.

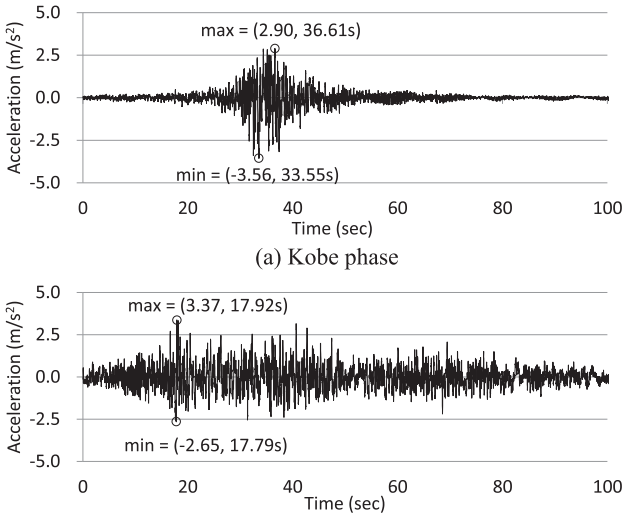

(a) Kobe phase

(b) Hachinohe phase

Fig. 10 Input acceleration waveforms at 75 m depth (2E)

Table 3 Numerical cases

Case	DMWs	No. of cells	A_r (%)	Input motion
K16	Yes	16	25	Kobe phase
H16	Yes	16	25	Hachinohe phase
K4	Yes	4	16	Kobe phase
H4	Yes	4	16	Hachinohe phase
K0	No	–	–	Kobe phase
H0	No	–	–	Hachinohe phase

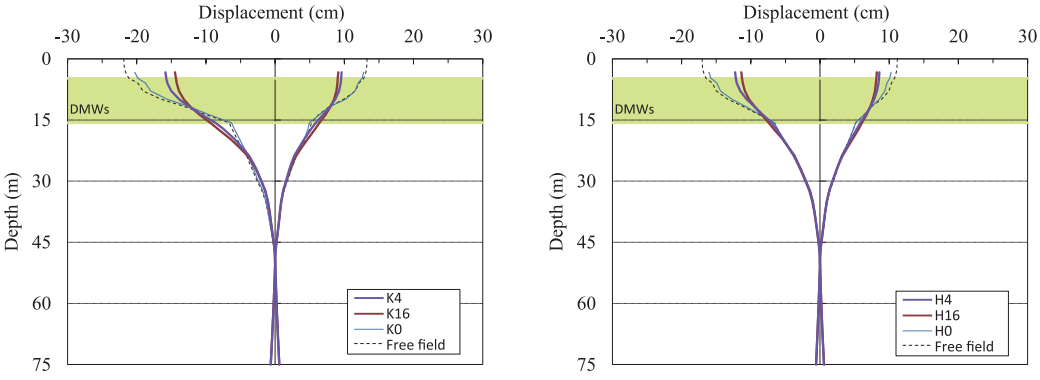

(a) Kobe phase

(b) Hachinohe phase

Fig. 11 Peak displacement profiles of ground at point A and free field

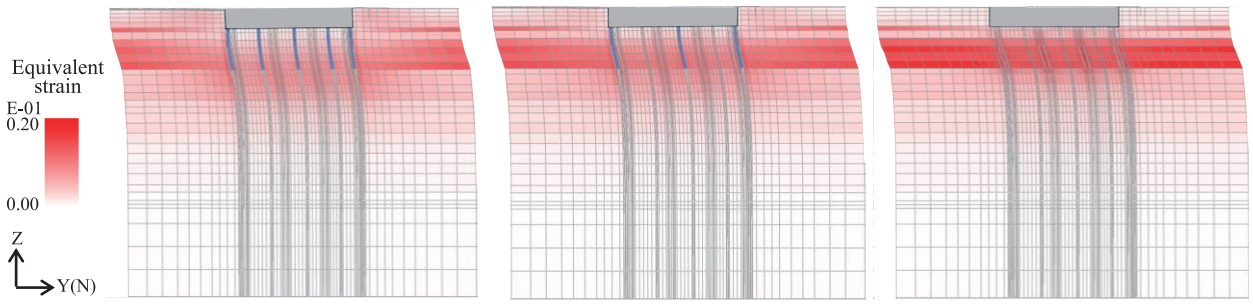

(a) K16

(b) K4

(c) K0

Fig. 12 Ground deformation with contours of equivalent strain at t_D (displacements enlarged by 25 times)

Figure 13 shows the peak equivalent strain profiles of the ground near the center of a cell together with those near the center of the raft in the cases without DMWs. The peak strains in the cases with 16 cells above the depth of the DMWs were decreased significantly compared to those in the cases without DMWs, and the maximum strains in the cases with four cells lie between them.

Figure 14 shows the bending moment histories in Piles 5B and 7B at the depth where the absolute maximum values were generated. In Pile 7B in K16, the time history at the 15.7 m depth is shown, while those at the pile head (at 4.8 m depth) are shown in the rest cases. The peaks of the bending moments in the case with DMWs were significantly smaller than those in the cases without DMWs.

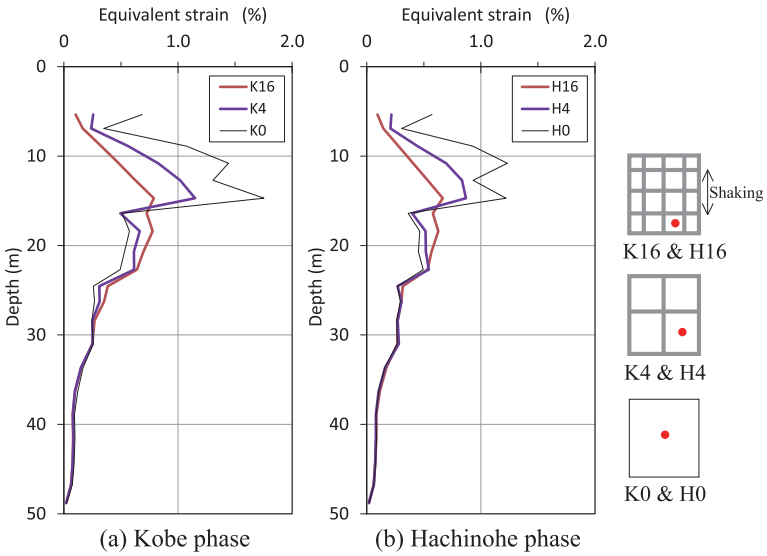

Fig. 13 Peak equivalent strain profiles of ground near center of a cell

The times when the absolute bending moment was its maximum in Piles 5B and 7B are referred as t_{M5B} and t_{M7B}, respectively, herein. The times of t_{M5B} and t_{M7B} were similar under each phase motion with one exception of t_{M5B} in Pile 5B in H4 which was late, 36.68 s. Note that the absolute maximum bending moment of Pile 5B in H4 at t_{M5B}=36.68 s (5.39 MN) was only slightly greater than that at t=18.66 s (5.38 MN) around which the absolute maximum moments in the other cases were generated.

Figure 15 shows the NS acceleration response spectra (5% damping) of the free-field ground surface and those of the raft bottom at point A. The response at the free field was obtained from the one-dimensional analysis using a soil column model. The amplification for the rafts was considerably lower than that for the free-field surface under both phase motions. It is seen that the amplification for the rafts with DMWs was lower than that for the rafts without DMWs in long period (1-2 s), and the amplification for the raft with four cells was slightly higher than that for the raft with 16 cells. The decrease in the acceleration response is presumed to have been caused mostly by the kinematic interaction among the raft, the DMWs and the soft soil.

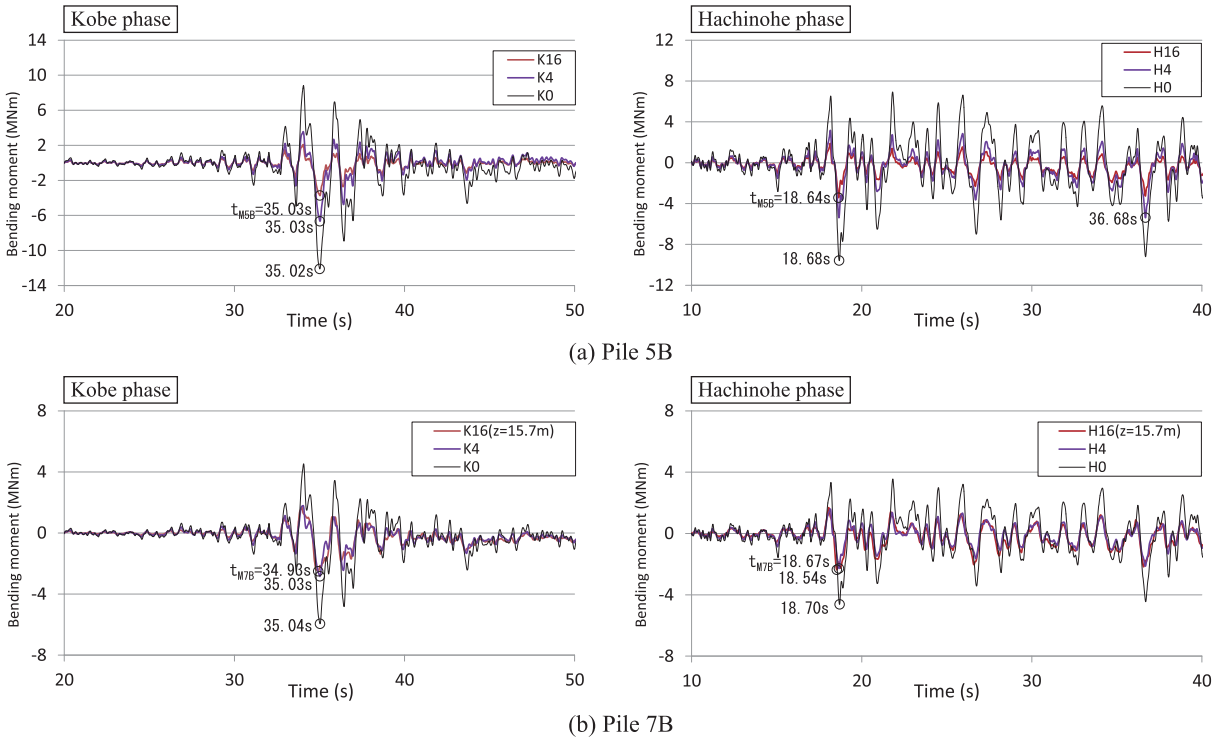

Fig. 14 Time history of bending moment in Piles 5B and 7B including the maximum

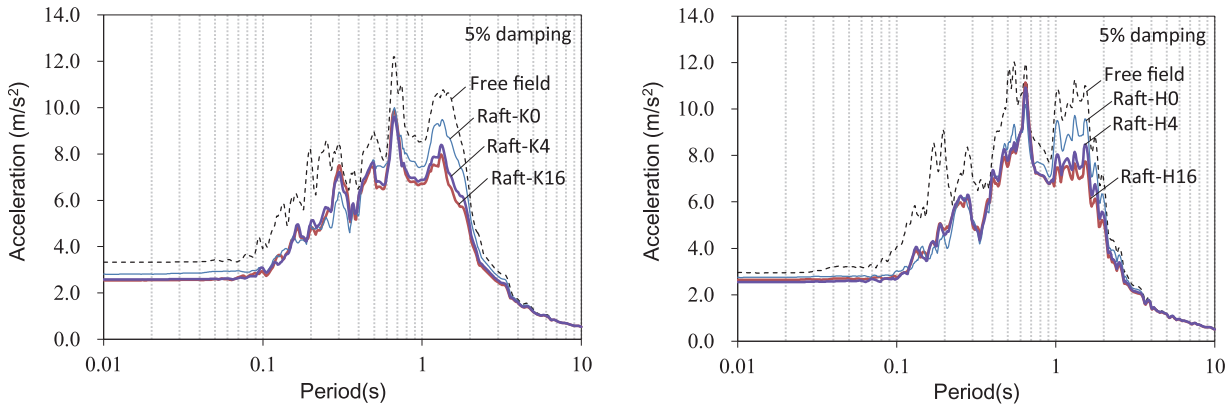

(a) Kobe phase (b) Hachinohe phase

Fig. 15 Acceleration response spectra: free-field surface and raft bottom at point A

4.2 Lateral load sharing in piled raft system

Figure 16 illustrates the equilibrium of the lateral external and resistant forces at the raft bottom under the Kobe phase at t_{M5B}. Regardless of the presence of the DMWs, the inertial forces of the superstructure and the raft were small compared to the

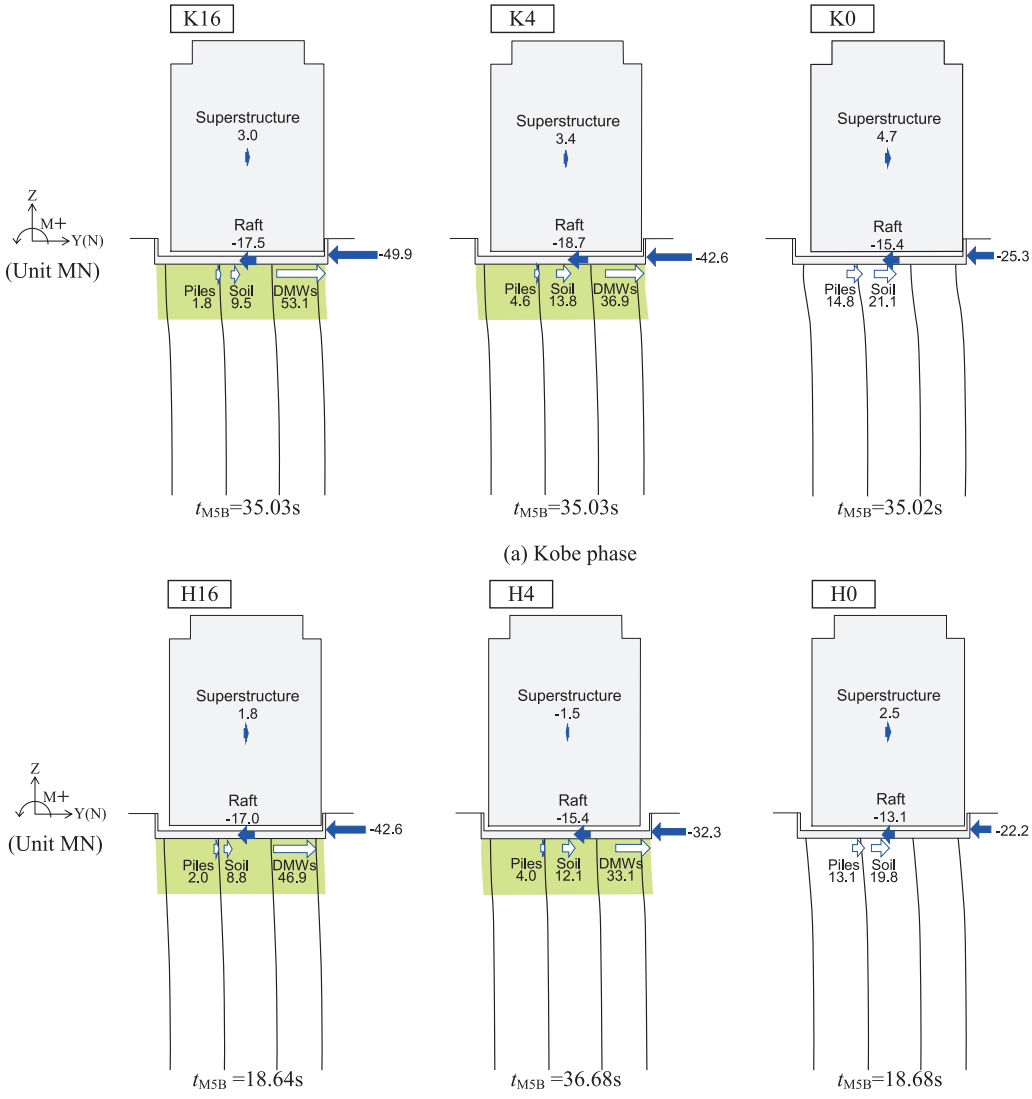

(a) Kobe phase

(b) Hachinohe phase

Fig. 16 Equilibrium of lateral forces at the raft bottom at t_{M5B} (displacements enlarged by 10 times for foundation while 5 times for superstructure)

earth pressure acting on the raft side. The earth pressure in the cases with DMWs was markedly large. This arises because the lateral stiffness of the raft with DMWs (of which bottom reached the stiffer clay) is much greater than that of the raft without DMWs although the lateral stiffness of the DMW grid with four cells is somewhat less than that with 16 cells. Hence, the total external forces acting at the raft bottom in K16 and K4 (64.3 and 58.0 MN, respectively) were significantly greater than that in K0 (35.9 MN). Here, the total external force acting at the raft bottom is the sum of the structure inertial force (the sum of the superstructure inertial force and the raft inertial force) and the earth pressure. In addition, the ratio of the lateral force carried by the DMWs to the total external force in K4 was slightly smaller than that in K16, i.e., 0.68 in the former and 0.83 in the latter. As a result, the loads carried by the piles in the cases with DMWs were very small (1.8-2.0 MN and 4.0-4.6 MN in the cases with four and 16 cells, respectively) compared to those carried by the piles in the cases without DMWs (13.1-14.8 MN).

4.3 Internal stresses in DMWs

Figure 17 illustrates the deformation of the DMW grids at t_{M5B}. Significant flexure due to bending is seen in the transverse walls (perpendicular to the shaking direction) near the bottom. Figure 18 illustrates the extent of the tensile failure in the DMW grid during the shaking. The elements are shaded according to the number of Gauss points at which the tensile failure occurs (total number of Gauss points in a single element is eight). The tensile failure occurred mostly in the longitudinal walls due to the shear deformation, while the failure near the bottom of the grid corners in the transverse walls would be caused by bending, as is seen in Fig. 17. The extent of the tensile failure in both grids under Hachinohe phase (H16 and H4) was larger than that under Kobe phase (K16 and K4), while the extent of the tensile failure in the grid with four cells was somewhat larger than that with 16 cells under both phase motions.

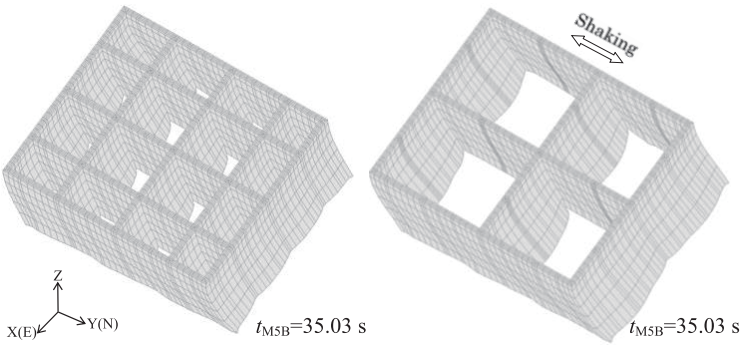

(a) K16 (b) K4

Fig. 17 Deformation of DMWs at t_{M5B} (displacements enlarged by 80 times)

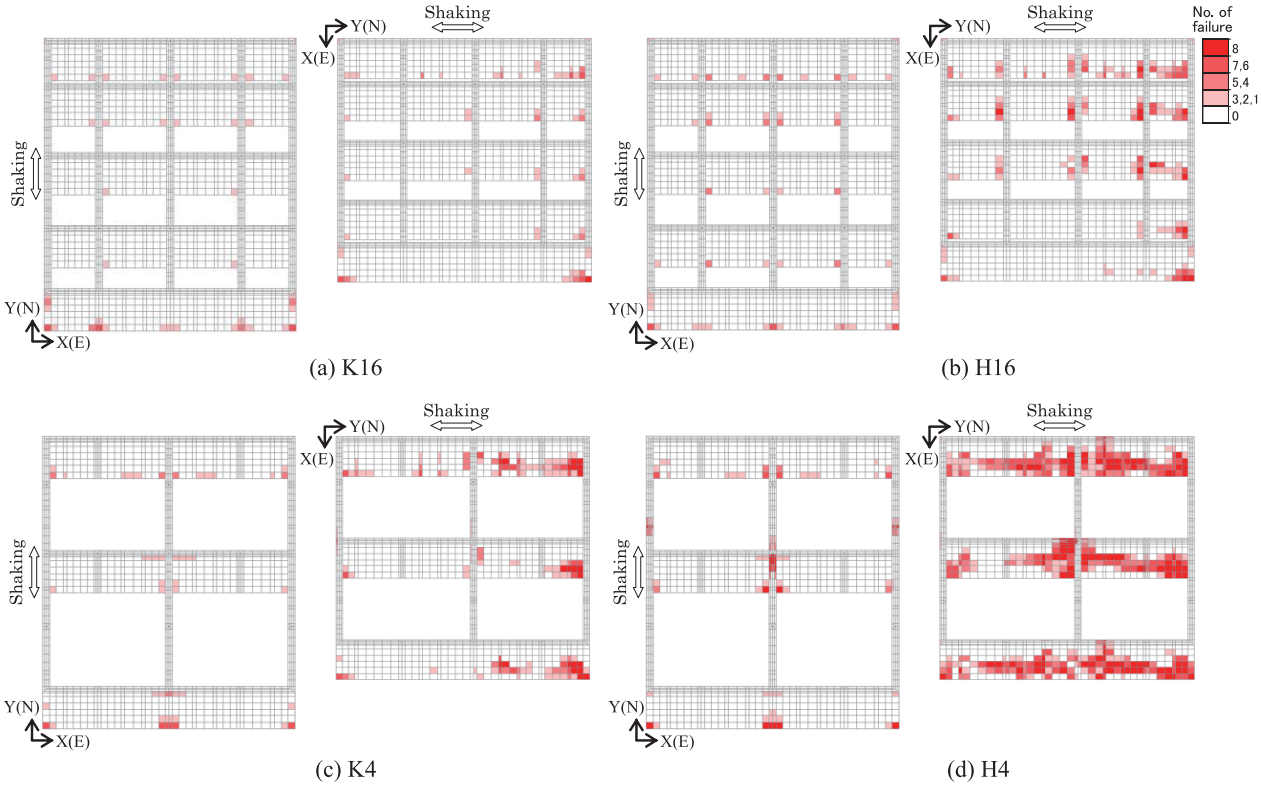

(a) K16 (b) H16

(c) K4 (d) H4

Fig. 18 Extent of tensile failure in DMW grid

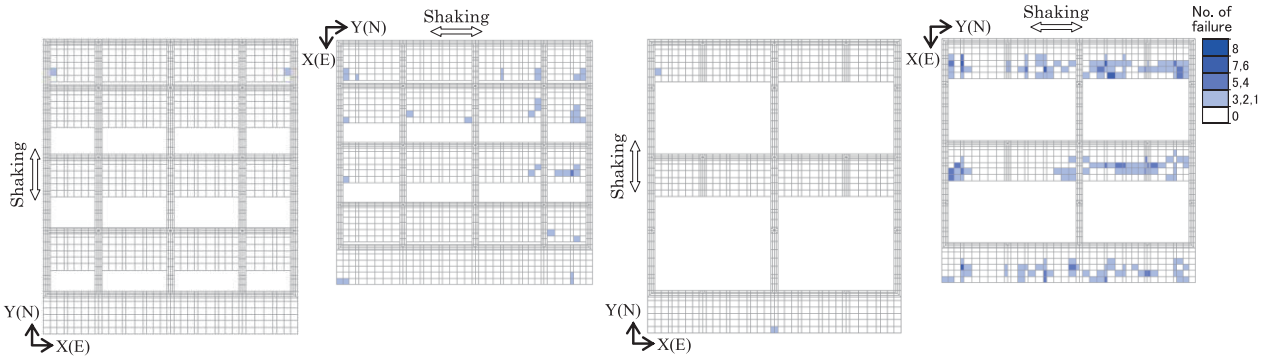

(a) H16 (b) H4

Fig. 19 Extent of shear failure in DMW grid (Hachinohe phase)

Figure 19 shows the extent of the shear failure in the DMW grids. The extent of the shear failure was very limited in comparison to that of the tensile failure. The shear failure in the grid with four cells was more conspicuous as was the tensile failure.

It should be noted that strain-softening characteristics of the stabilized soil may appear after the tensile stress reaches the tensile strength, as pointed out by Namikawa et al. (2007). Shigeno et al. (2018) performed the numerical analysis for the case of H16 (denoted in this paper) using the constitutive model of the stabilized soil which is able to evaluate the post-peak tension-softening, and showed that although the extent of the tensile failure in the case with softening was fairly large compared to that in the case without softening, the maximum bending moments of the piles were similar between them. However, further analytical studies on the strain-softening characteristics would be necessary in order to clarify the seismic behavior of the DMWs under strong earthquakes more accurately. Furthermore, physical modelling, such as a geotechnical centrifuge (Khosravi et al., 2016; Hamada et al., 2017), would also be required to verify the numerical analysis results.

4.4 Pile bending moments

Figure 20 shows the peak bending moment profiles of Piles 5B and 7B under the rigid connection between the piles and the raft.

The bending moments near the pile head in the cases with DMWs were significantly smaller than those in the cases without DMWs. The bending moment in the cases with four cells were slightly greater than those in the cases with 16 cells under both phase motions. In the cases with DMWs, relatively large bending moments were generated around a depth of the grid bottom in Pile 7B, while the maximum bending moments were generated at the pile head in Pile 5B. This is discussed below.

Figure 21 shows the snapshots of the horizontal displacement relative to the reference point (at 49.9 m depth) and the bending moments in Pile 5B at t_{M5B} and those in Pile 7B at t_{M7B}. Note that the horizontal displacements in Pile 5B in H4 were somewhat smaller than those in H16 because t_{M5B} in H4 was quite different from those in the other cases as shown in Fig. 14.

In the cases with DMWs under both phase motions, the bending moments in Pile 7B were relatively large at a depth of the grid bottom and the maximum moments in K16 and H16 were generated at the depth of the grid bottom while the bending moments in Pile 5B decreased generally with depth. The difference in the moment distribution arises probably due to the following mechanism: Since Pile 7B is located more closely to the grid wall than Pile 5B, the constraint of the lateral deformation of Pile 7B by the soil confined in the grid might be more pronounced than that of Pile 5B. As a result, the kinematic effect arising from the ground movement around the depth of the grid bottom, at which lateral subgrade reaction coefficient of the pile changes abruptly, would lead to significant increase in the bending moment in Pile 7B. In addition, since the rigidity of the DMW grid with 16 cells is greater than that with four cells, the restraint of the piles in the former cases would be more pronounced than that in the latter cases. Consequently, the maximum bending moment in Pile 7B in the cases with 16 cells were generated at the depth of the grid bottom. Thus, it was found that the distribution of the bending moment depends on the location of pile in the grid as well as the rigidity of the grid.

Figure 22 shows the relationship between the axial force and the absolute maximum bending moment along the pile, together with the design interaction curves of the SC pile. Here, the axial force was assumed to be the sum of the pile head load (which

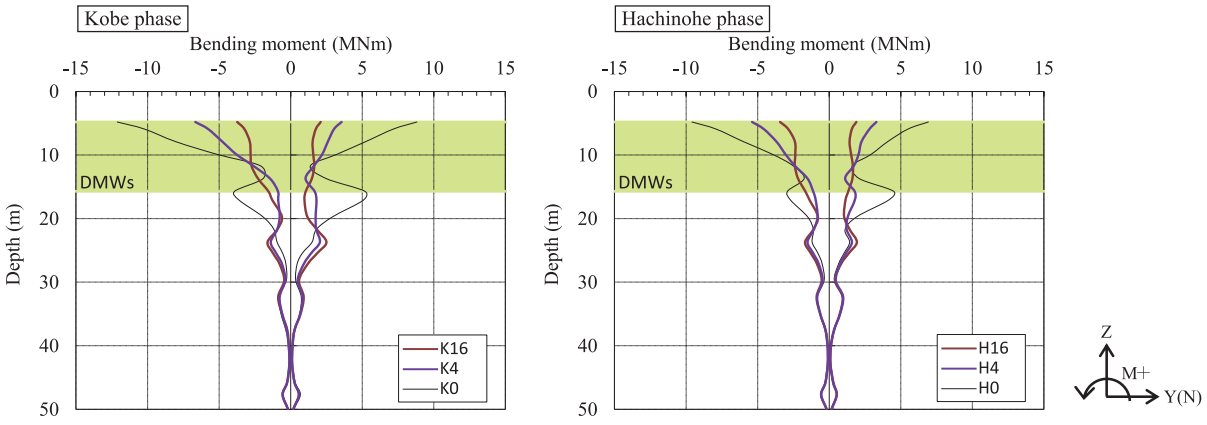

(a) Pile 5B

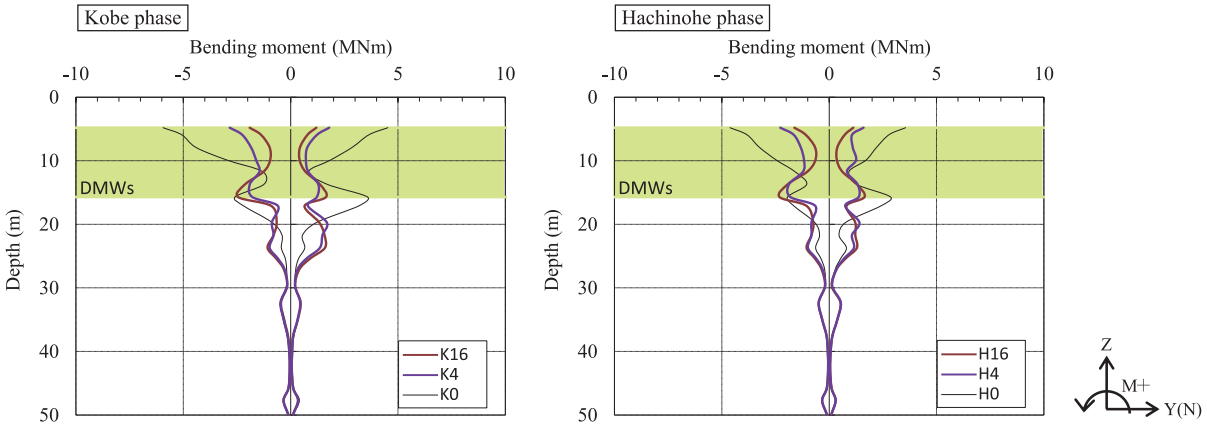

(b) Pile 7B

Fig. 20 Peak bending moment profiles

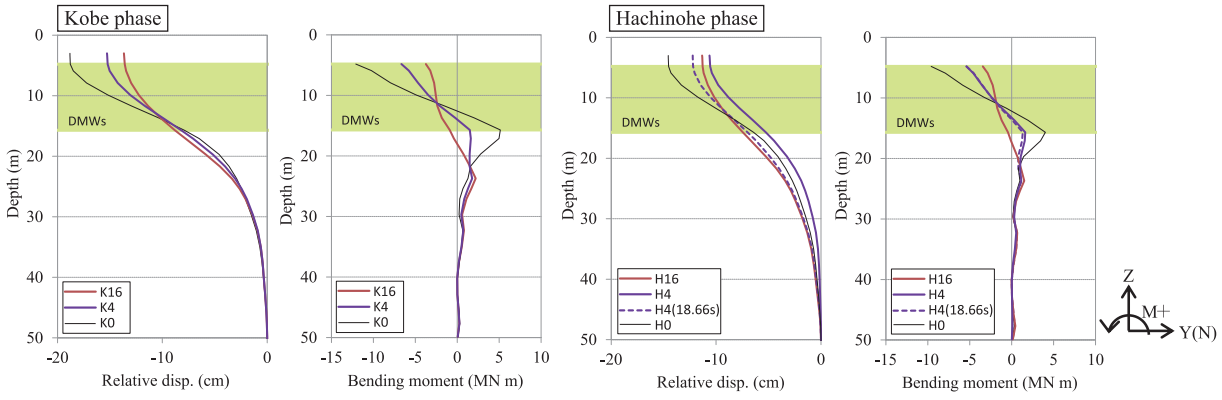

(a) Pile 5B (at t_{M5B})

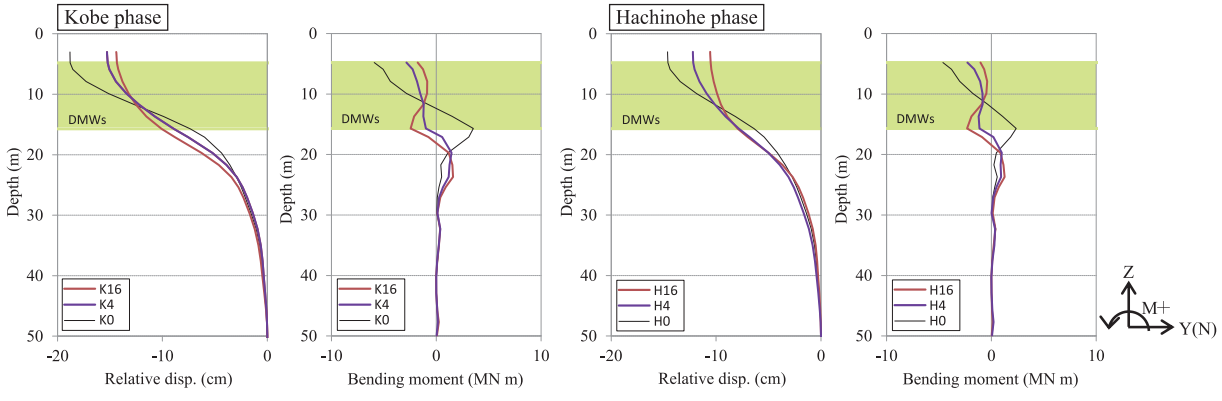

(b) Pile 7B (at t_{M7B})

Fig. 21 Snapshots of horizontal displacement and bending moment in Piles 5B and 7B

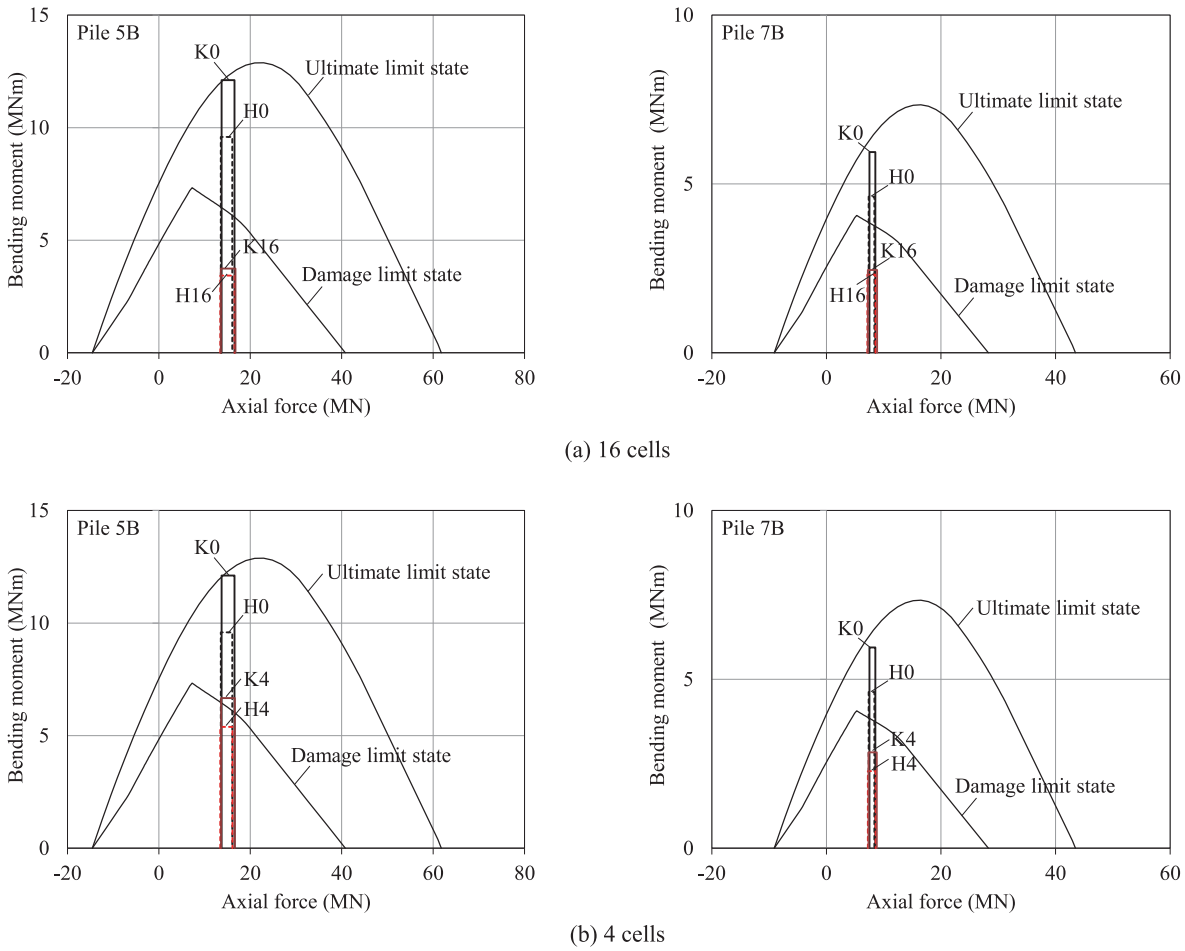

(a) 16 cells

(b) 4 cells

Fig. 22 Absolute maximum moment along pile with design NM-interaction curves of SC piles

was measured just before the 2011 Tohoku Earthquake) and the maximum and minimum dynamic incremental force obtained from the analysis. In order to examine the performance of the piles from a point of view of engineering practice, the design interaction curves for bending moment and axial load are also shown in Fig. 22. Here, the ultimate limit state means that the unit stress at the edge of the concrete reaches the compressive strength, while the damage limit state means that the unit stress at the edge of the concrete is almost in the elastic condition.

It is seen that the maximum bending moments in the cases with four cells were around the damage limit state under both phase motions, and significantly below the ultimate limit state under Level 2 seismic motion. The bending moments in cases with 16 cells were fairly below the damage limit state under Level 2 seismic motion while those in the cases without the DMWs were close to the ultimate limit state, as presented in the previous paper.

5 CONCLUSIONS

The effects of the DMWs on the seismic response of the piled raft system under Level 2 seismic motions were investigated. Through the investigations, the following conclusions can be drawn:

(1) When the bending moment at the pile head in Pile 5B was at its maximum (at t_{M5B}), the total external forces acting at the raft bottom in the cases with DMWs were significantly greater than those in the cases without DMWs because the earth pressure acting on the raft side was markedly large in the cases with DMWs. The ratio of the lateral force carried by the DMWs to the total external force in the cases with four cells was slightly smaller than that in the cases with 16 cells. As a result, the loads carried by the piles in the cases with four cells were slightly large compared to those carried by the piles in the cases with 16 cells.

(2) The extent of the tensile failure in the longitudinal walls in the cases with four cells was somewhat larger than that with 16 cells under both phase motions, and the maximum bending moments of the piles in the former were slightly greater

than those in the latter. Nevertheless, the maximum bending moment of the piles in the cases with four cells were found to be significantly below the ultimate limit state. It should be noted that the bending moments in the cases with 16 cells were fairly below the damage limit state, as presented in the previous paper.

ACKNOWLEDGEMENTS

The authors are grateful to Prof. T. Namikawa of Shibaura Institute of Technology for his contribution to the constructive comments on the numerical simulation analysis.

REFERENCES

Bradley, B. A., Araki, K., Ishii, T., Saitoh, K., 2013. Effect of lattice-shaped ground improvement geometry on seismic response of liquefiable soil deposits via 3-D seismic effective stress analysis, Soil Dynamics and Earthquake Engineering, Vol. 48, 35-47.

Building Center of Japan, 2002. Specification for design and quality control of cement treated soil (in Japanese).

Building Standard Law of Japan, 2000. Notification No. 1461 of the Ministry of Construction (in Japanese).

Hamada, J., Shigeno, Y., Onimaru, S., Tanikawa, T., Nakamura, N., Yamashita, K., 2014. Numerical analysis on seismic response of piled raft foundation with ground improvement based on seismic observation records, Proc. of the 14th IACMAG, Kyoto.

Hamada, J. and Honda, T., 2017. Centrifuge model tests on failure behavior of grid-form deep mixing walls during large earthquake, the 16thWCEE.

Katzenbach, R., Arslan, U., Moormann, C., 2000. Piled raft foundation projects in Germany, Design applications of raft foundations, Hemsley J.A. Editor, Thomas Telford, 323-392.

Khosravi, M., Boulanger, R. W., Tamura, S., Wilson, D. W., Olgun, C. G. and Wang, Y., 2016. Dynamic centrifuge tests of soft clay reinforced by soil-cement grids, J. Geotech. Geoenviron. Eng. 142(7), ASCE.

Kitazume, M., 2013. Deep mixing method in Japan, Geotechnical Engineering Journal of the SEAGS & AGSSEA, Vol. 44, No.4, 97-114.

Kuroda, T., Tanaka, H., Tomii, Y., Suzuki, Y., 2001. Evaluation of characteristics of improved soil by the deep mixing method of soil stabilization, Study on dynamic deformation characteristics of improved soil (Part 3), Summaries of technical papers of annual meeting AIJ, B-1, 699-700 (in Japanese).

Mandolini, A., Russo, G., Viggiani, C., 2005. Pile foundations: Experimental investigations, analysis and design, Proc. of the 16th ICSMGE, Osaka, Vol. 1, 177-213.

Motojima, M., Hibino S. and Hayashi, M., 1978. Development of computer program for stability analysis of excavation, Central Research Institute of Electric Power Industry Report No 377012 (in Japanese).

Namikawa, T., Koseki, J. and Suzuki, Y., 2007. Finite element analysis of lattice-shaped ground improvement by cement-mixing for liquefaction mitigation, Soils & Foundations, Vol. 47 (3), 559-576.

Poulos, H. G., 2001. Piled raft foundations: Design and applications, Géotechnique, Vol. 51(2), 95-113.

Shigeno, Y., Hamada, J., Nakamura, N., 2014. Hybrid parallelization of earthquake response analysis using K computer, Proc. of the 14th IACMAG, Kyoto.

Shigeno, Y., Yamashita, K., Hamada, J., 2018. Seismic performance of a piled a raft foundation with grid-form DMWs considering softening of stabilized soil, Proc. of Int. Conf. on Deep Foundations and Ground Improvement.

Shiomi, T., Shigeno, Y. and Zienkiewicz, O. C., 1993. Numerical prediction for model No. 1. Verification of Numerical Procedures for the Analysis of Soil Liquefaction Problems (eds. by Arulanandan & Scott), Balkema, 213-219.

Tsujino, S., Yoshida, N. and Yasuda, S., 1994. A simplified practical stress-strain model in multi-dimensional analysis, Proc. of International Symposium on Pre-failure Deformation Characteristics of geomaterials, Sapporo, 463-468.

Verdugo, R., 2017. Seismic site classification, Proc. of the 3rd International Conference on Performance-based design in Earthquake Geotechnical Engineering, PBDⅢ, Vancouver, 526.

Yamashita, K., Yamada, T., Hamada, J., 2011a. Investigation of settlement and load sharing on piled rafts by monitoring full-scale structures, Soils & Foundations, Vol. 51 (3), 513-532.

Yamashita, K., Hamada, J., Yamada, T., 2011b. Field measurements on piled rafts with grid-form deep mixing walls on soft

ground, Geotechnical Engineering Journal of the SEAGS & AGSSEA, Vol. 42 (2), 1-10.

Yamashita, K., Hamada, J., Onimaru, S., Higashino, M., 2012. Seismic behavior of piled raft with ground improvement supporting a base-isolated building on soft ground in Tokyo, Soils & Foundations, Vol. 52 (5), 1000-1015.

Yamashita, K., Wakai, S. and Hamada, J., 2013. Large-scale piled raft with grid-form deep mixing walls on soft ground, Proc. of the 18th Int. Conference on SMGE, Paris, 2637-2640.

Yamashita, K., Hamada, J., Tanikawa, T., 2016. Static and seismic performance of a friction piled raft combined with grid-form deep mixing walls in soft ground, Soils & Foundations, Vol. 56 (3), 559-573.

Yamashita, K., Uchida, A., Tanikawa, T., 2017. Long-term behavior of friction piled raft with grid-form DMWs in loose sand underlain by thick clay layers in reclaimed land, Proc. of the 19th Int. Conference on SMGE, Seoul, 2885-2888.

Yamashita, K., Shigeno, Y., Hamada, J., Chang, D. W., 2018. Seismic response analysis of piled raft with grid-form deep mixing walls under strong earthquakes with performance-based design concerns, Soils & Foundations, Vol. 58 (1), 65-84.